Zinc Lowers Amyloid-β Toxicity by Selectively Precipitating Aggregation Intermediates †

5 AUTHORS, INCLUDING:

Kanchan Garai
TIFR Centre for Interdisciplinary Sciences
30 PUBLICATIONS **710** CITATIONS

SEE PROFILE

Sanjeev Kaushalya
Max Planck Institute for Medical Research
14 PUBLICATIONS **176** CITATIONS

SEE PROFILE

Radha Desai
University College London
5 PUBLICATIONS **136** CITATIONS

SEE PROFILE

Sudipta Maiti
Tata Institute of Fundamental Research
83 PUBLICATIONS **2,523** CITATIONS

SEE PROFILE

Zinc Lowers Amyloid-β Toxicity by Selectively Precipitating Aggregation Intermediates[†]

K. Garai, B. Sahoo, S. K. Kaushalya, R. Desai,[‡] and S. Maiti*

Department of Chemical Sciences, Tata Institute of Fundamental Research, Homi Bhabha Road, Colaba, Mumbai 400005, India

Received January 17, 2007; Revised Manuscript Received June 27, 2007

ABSTRACT: Soluble amyloid-β (Aβ) aggregates are suspected to play a major role in Alzheimer's disease. Zn^{2+} at a concentration of a few micromolar, which is too dilute to affect the precipitation equilibrium of Aβ, can destabilize these aggregates [Garai, K., Sengupta, P., Sahoo, B., and Maiti, S. (2006) *Biochem. Biophys. Res. Commun. 345*, 210−215]. Here we investigate the nature of these aggregates in the context of the precipitation pathway, the mechanism underlying their destabilization, and the biological consequences of this destabilization. We show that the larger soluble aggregates (size > 10 nm) form only in supersaturated Aβ solutions, implying that they are intermediates in the pathway toward fibril formation. We also show that Zn^{2+} destabilizes these intermediates by accelerating their aggregation kinetics. The resulting change in the size distribution of the Aβ solution is sufficient to eliminate its toxicity to cultured mammalian neurons. Our results provide an explanation for the existing observations that Zn^{2+} at a concentration of a few micromolar significantly reduces Aβ toxicity.

Aggregation of the amyloid Aβ[1] peptide causes deposits ("plaques") of insoluble Aβ fibrils in the brain, which is an invariant feature of Alzheimer's disease (AD). However, recent experiments suggest that the soluble oligomeric species of Aβ (*1−5*), and not the insoluble precipitates, are the key toxic agents in AD. The total soluble Aβ load in the brain (especially that of A$\beta_{1−40}$) has been found to be a better predictor of the severity of AD compared to the amount of insoluble Aβ deposits (*6*).

In vitro, depending on the method of preparation, various aggregates of different shapes and sizes are found in Aβ solutions: low molecular weight oligomers, high molecular weight but still soluble Aβ aggregates, and insoluble amyloid fibrils (*3, 4, 7, 8*). Cryoelectron microscopy of mutant Aβ species found in a familial form of AD has pointed toward oligomers with 7−11 nm large ringlike structures (*2*) as the key agents of toxicity, while other studies have held spherical oligomers (size > 10 nm) (*3*) responsible. Smaller oligomers (containing only a few monomers) have also been found to be potent disruptors of LTP in hippocampal neurons (*9*). It is not clear which of these aggregates are kinetic intermediates in the pathway of precipitation (which would only form above the saturation concentration (C_{sat}), (*10*) and which can remain in equilibrium with the monomers (which can exist even below C_{sat}). This question is critical because if the toxic aggregates are kinetic intermediates, a strategy to catalytically modify the kinetics of aggregation can effectively alter their population. Here we address this question by measuring the size distribution of the heterogeneous mixture of soluble Aβ particles using fluorescence correlation spectroscopy (*11*) as a function of Aβ concentration.

An ideal AD treatment would selectively eliminate the soluble aggregate species. Some chemical agents (*12, 13*) can eliminate the soluble aggregates and are promising candidates for AD therapy. We have recently shown that Zn^{2+} at a few micromolar concentration can also destabilize the larger soluble aggregates (*14*), though the mechanism remains unclear. Here we investigate the destabilization pathway and the possible molecular mechanism underlying it. We also investigate whether this Zn^{2+}-induced elimination of the soluble aggregates leads to a change in the toxicity of Aβ. The role of Zn^{2+} in AD has been controversial. Zn^{2+} binds Aβ and promotes its precipitation (*15, 16*), and AD plaques in the brain are found to be rich in Zn^{2+} (*17*). Also, genetic ablation of synaptic Zn^{2+} prevents Aβ deposition (*18*). Zn^{2+} at high concentrations promotes Aβ-induced toxicity in vitro (*19*) and also in vivo (*20*). However, studies that report an increased toxicity at high (1 mM) Zn^{2+} concentrations also report a neuroprotective effect at lower (<50 μM) concentrations (*19, 21−23*). This concentration-dependent role of Zn^{2+} in Aβ-associated neurotoxicity has been termed a paradox (*24*). We investigate whether the effect of low concentrations of Zn^{2+} can be understood in terms of specific interactions of Zn^{2+} with the soluble Aβ aggregates.

[1] Abbreviations: Aβ, amyloid-β peptide (residues 1−40); RAβ, Rhodamine-labeled Aβ; AD, Alzheimer's disease; C_{sat}, saturation concentration; FCS, fluorescence correlation spectroscopy; MEMFCS, maximum entropy method based algorithm to analyze FCS data; EDTA, ethylenediaminetetraacetic acid; EM, electron microscopy; AFM, atomic force microscopy.

EXPERIMENTAL PROCEDURES

FCS Measurements. $A\beta_{1-40}$ and fluorescent TAMRA-K-$A\beta_{1-40}$ ($RA\beta$) are purchased from RPeptide (Athens, GA). $A\beta_{1-40}$ is dissolved in HEPES buffer (20 mM HEPES, 146 mM NaCl, 5.4 mM KCl) at pH 7.4 to final concentrations of 2, 10, and 50 μM. $RA\beta$ (100 nM final concentration) is added to this solution, and the solution is incubated at room temperature for 10 h. For the Zn^{2+} experiments, 8 μM $ZnCl_2$ is added to the $A\beta$ solution at a specific time prior to the measurement. The solution is then used for FCS measurements or for toxicity assays. We add a drop of 80 μM $ZnCl_2$ solution to dilute it in the $A\beta$ solution to the final concentration of 8 μM Zn^{2+}. We shake all solutions continuously. The 50 μM $A\beta$ solutions are lightly centrifuged (2000g for 20 min) at 2 h to eliminate the very large particles which otherwise interfere with FCS measurements. Less than 10% of $A\beta$ precipitates at this step. For the experiments with ethylenediaminetetraacetic acid (EDTA), 20 μM EDTA was added online with the Zn^{2+}-incubated $A\beta$ sample. All the chemicals, unless mentioned, are purchased from Sigma Chemicals, St. Louis. The salts used for buffer preparation are recrystallized twice to get rid of trace impurities. The FCS measurements are performed with a home-built FCS spectrometer as described elsewhere (*25*).

Transmission Electron Microscopy (TEM). A 50 μM $A\beta$ solution is prepared and incubated at room temperature (rt) for 24 h. For the Zn^{2+} experiment 8 μM (final concentration) $ZnCl_2$ is added after 2 h of preparation of the $A\beta$ solution, which is then incubated at rt for 22 h. For each specimen one droplet is put on a Formvar-coated 100 mesh copper grid and is allowed to be adsorbed for 2–3 min. The extra amount is removed with tissue paper. Then a drop of 0.1% uranyl acetate is added to the grid and is left for 5 min for staining. The extra uranyl acetate is removed by tissue paper, and the grids are left under an infrared lamp for drying. The specimen is then analyzed with a transmission electron microscope (Zeiss, model no. 109).

Toxicity Assay. The cells are taken from the raphe region of 2 day old Wistar rat brains (*26*) and cultured in Petri dishes for 5 days using standard protocols. They are incubated in the $A\beta$ solutions for 9 h (4 h for 50 μM $A\beta$) at 37 °C and subsequently with 0.01 mg/mL Hoechst and 0.01 mg/mL propidium iodide (PI) solutions for 10 min. The cells are then washed with modified Thomson's buffer (20 mM HEPES, 146 mM NaCl, 5.4 mM KCl, 2.3 mM $CaCl_2$, 0.4 mM KH_2PO_4, 0.3 mM Na_2HPO4, 5 mM glucose), placed under an upright microscope (Nikon ECLIPSE E600FN), and imaged with a 20× objective. All buffers and salts are purchased from SD Fine Chemicals, India. The images of the cells are captured with a cooled CCD camera (IXON DV887, Andor, U.K.). All animal handling protocols are approved by the institutional animal ethics committee.

Statistical Analysis. Several images with a viewing area of 400 μm × 400 μm are recorded from each dish. The number of dead (PI-labeled) and total (Hoechst-labeled) cells are then counted in each of the image fields. The mean and the standard error of the mean (SEM) are calculated from these individual numbers. Student's *t* test is performed (two-tailed) to test the significance of the difference of the mean number of deaths from different samples. Even though the distribution is inherently binomial, it is expected to ap-

proximate a normal distribution for the large n values used here. A total of five image fields (total number of cells $n = 1723$) for 10 μM $A\beta_{1-40}$ treated samples, six for 10 μM $A\beta_{1-40}$ + Zn^{2+} treated ($n = 1035$) samples, eight for 2 μM $A\beta_{1-40}$ ($n = 448$) samples, and four for control ($n = 628$) samples are used for this calculation. For the death assay with 50 μM $A\beta_{1-40}$, a total of 15 image fields (total number of cells $n = 2626$) for $A\beta_{1-40}$ treated samples, 12 for $A\beta_{1-40}$ + Zn^{2+} treated ($n = 2056$) samples, and 12 for control ($n = 1438$) samples are used for this calculation. It is assumed that the sample sizes are small. For calculating the confidence limits, we perform Student's *t* test with degrees of freedom (*f*) given by (*27*)

$$f = \cfrac{1}{\cfrac{u^2}{n_1 - 1} + \cfrac{1 - u^2}{n_2 - 1}}$$

where

$$u = \frac{SEM_1{}^2}{SEM_1{}^2 + SEM_2{}^2}$$

The degrees of freedom *f* reduces to the familiar value of $n_1 + n_2 - 2$ if the SEM values are not significantly different.

RESULTS

To characterize the soluble $A\beta$ species across the size range, we measure the size distribution of $A\beta$ particles in vitro at different $A\beta$ concentrations using fluorescence correlation spectroscopy (FCS) (*25*). We investigate HEPES-buffered aqueous solutions at pH 7.4 containing 2 μM $A\beta$ and 10 μM $A\beta$ (with 100 nM Rhodamine B-labeled $A\beta$ present in both the solutions as a reporter molecule). We use HEPES as a buffer here to avoid Zn^{2+} solubility problems in phosphate buffers. We have previously shown that $A\beta$ has a well-defined saturation concentration in aqueous solutions (*10*). We determine that the saturation concentration of $A\beta$ in HEPES-buffered solutions is about 4 μM, using fluorescence of the tyrosine residue as a reporter of the $A\beta$ concentration (using the same method as described in ref *10*). A 10 μM $A\beta$ solution in HEPES is supersaturated, in which precipitation will continue until the concentration reduces to saturation. On the other hand, a 2 μM $A\beta$ solution is unsaturated, in which precipitation is not expected. FCS measurements are performed 10 h after the preparation of the solutions (it takes several days for the precipitation to be complete). The fluorescence photon count traces (which constitute the raw data for FCS) obtained from a 10 μM $A\beta$ solution before and 30 min after addition of 8 μM Zn^{2+} are shown in parts a and b, respectively, of Figure 1. Figure 1a shows a large number of fluorescent spikes, originating from the larger soluble aggregates, compared to Figure 1b. The correlation traces are shown in Figure 1c (green for 2 μM $A\beta$, blue for 10 μM $A\beta$ before addition of Zn^{2+}, and red for the same solution after addition of Zn^{2+}). For comparison, the corresponding data obtained from a 10 nM aqueous solution of Rhodamine B is shown in black. The data are fitted (solid lines) in a bias-free manner by a quasi-continuous distribution of particle sizes with the maximum entropy method based algorithm MEMFCS (*11*). The size distribu-
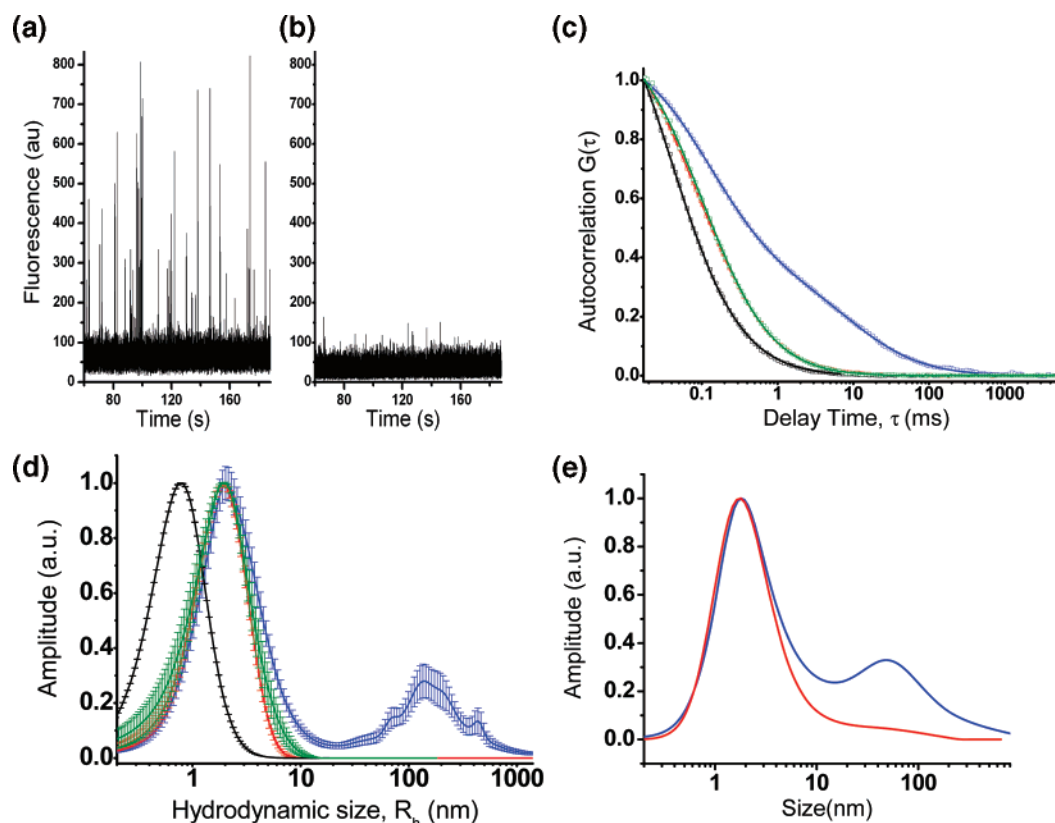
FIGURE 1: Zn^{2+} eliminates soluble aggregates from amyloid-β solutions. Fluorescence data averaged for 2 ms at each time point for (a) 10 μM Aβ solution and (b) 10 μM Aβ + 8 μM Zn^{2+} solution, respectively. (c) Normalized fluorescence autocorrelation data calculated as a function of the delay time (scattered points) and the corresponding fits (solid lines) for 2 μM Aβ (green), 10 μM Aβ (blue), 10 μM Aβ + 8 μM Zn^{2+} (red), and Rhodamine B (black) solutions. (d) Size distribution obtained from (c) (same color code as in (c)). The abscissa is calibrated with reference to Rhodamine B. The ordinate shows the population weighted by the square of the brightness of individual particles. (e) Size distribution of 50 μM Aβ solution before (blue) and after (red) centrifugation at 14000g for 20 min. Centrifugation leads to a size-dependent reduction of the second peak.

tions obtained from the fits are shown in Figure 1d. The error bars shown with the size distribution curves are obtained from 10 identical measurements for each sample. The size (hydrodynamic radius) axis is calibrated by using Rhodamine B as a standard (hydrodynamic radius of 0.78 nm) (Figure 1d, black). The ordinate represents the population of a species weighted by the square of its fluorescence intensity (per particle) (*11*). The 2 μM Aβ size distribution shows a single peak (Figure 1d, green) at 2.0 nm which is close to the calculated size of the monomers (1.8 nm, using a spherical approximation). The 10 μM Aβ size distribution shows two distinct peaks (Figure 1d, blue). The first peak is at ∼2.1 nm, representing monomers and dimers. The size distribution near this peak is broader toward higher particle sizes compared to that of 2 μM Aβ. The second peak is broad and contains particles of hydrodynamic sizes larger than 10 nm and ranging up to 300 nm. These particles are never observed in subsaturated solutions. When 8 μM Zn^{2+} is present in the solution together with 10 μM Aβ, the second peak disappears (Figure 1d, red; Figure 1b shows the corresponding fluorescence data, and Fibure 1c shows the correlation trace and the fit), consistent with the observations made earlier (*14*). In addition, we observe that the first peak also shrinks to an extent that the total size distribution now appears to overlap that of the unsaturated 2 μM solution (see the autocorrelation curve, as well as the resultant distribution). This indicates that all the larger particles have been destabilized by Zn^{2+}. It is possible to check the reliability

of the FCS measurements using strong centrifugation. If the second peak in FCS indeed corresponds to particles of higher mass, then centrifugation of the solution should also reduce this peak. We centrifuge a separate preparation of 50 μM Aβ solution at 14000g for 20 min. The size distribution before (blue) and after (red) centrifugation is shown in Figure 1e. A size-dependent reduction in the population of the large soluble aggregates is observed (Figure 1e, red), consistent with the expected precipitation of the higher mass particles. Therefore, the species specifically destabilized by Zn^{2+} are indeed the higher mass aggregates.

Next we investigate whether this Zn^{2+}-induced disappearance of the soluble aggregates is due to their aggregation and subsequent precipitation or due to their dissolution back into the monomeric state. In thermodynamic terms, it can signify a reduction of the height of the free energy barrier separating the monomers/small oligomers and the larger soluble aggregates or that separating the larger soluble aggregates and the precipitate state. We investigate which of these possibilities is actually true. We measure the size distribution of a 10 μM Aβ solution 4 h after its preparation. We then add 8 μM Zn^{2+} and follow the evolution of the particle size distribution as a function of time. The kinetics of the size distribution is shown in Figure 2a. The average size of the soluble aggregate species before zinc addition is measured to be 130 nm (Figure 2a, solid line). Within 15 min of zinc addition the average size (∼250 nm) and the relative population of the aggregates increase (Figure 2a,
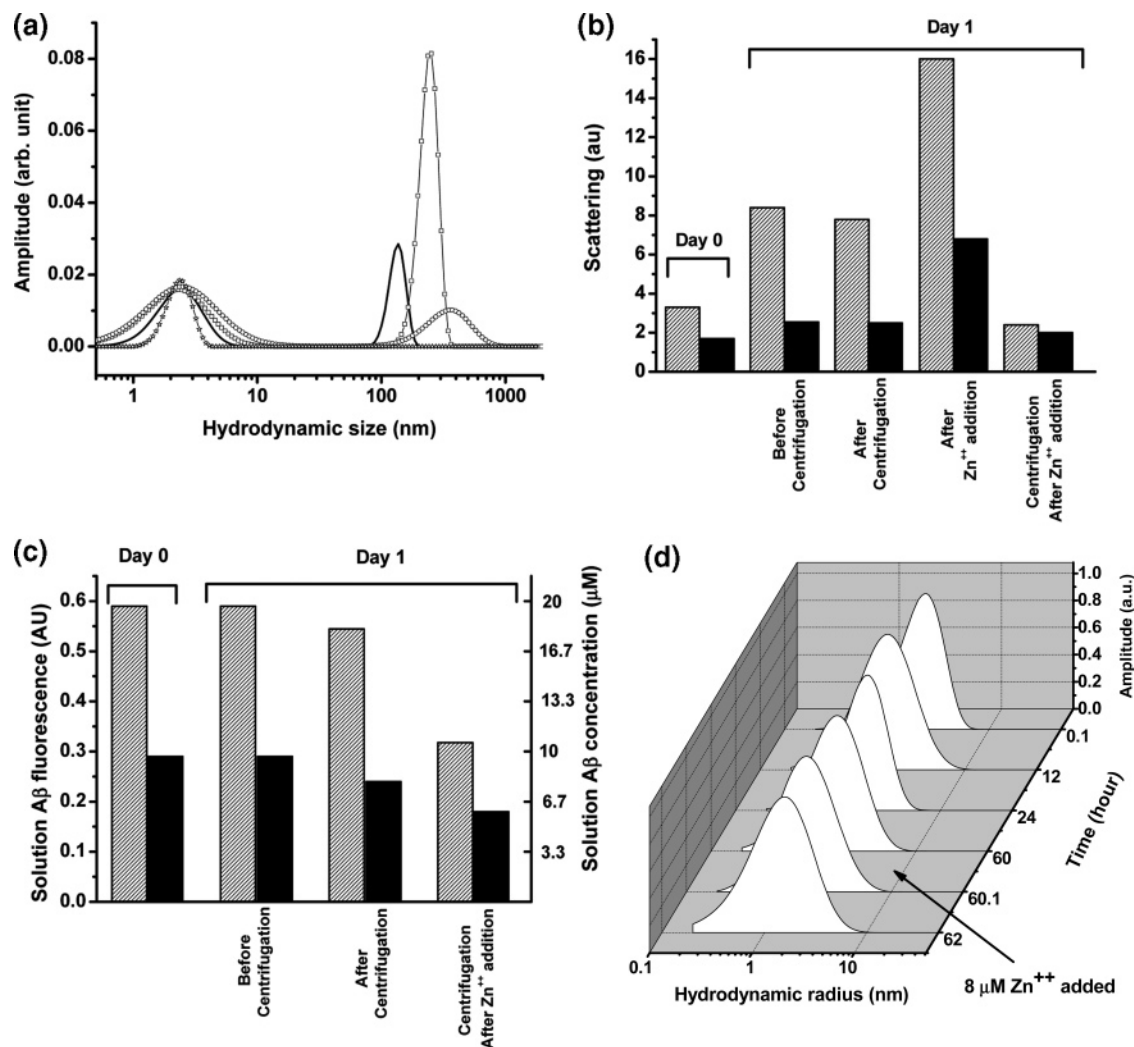
FIGURE 2: Zn^{2+} eliminates soluble aggregates by precipitation. (a) Kinetics of interaction of Zn^{2+} with aggregates in 10 μM Aβ solution measured with FCS. Size before Zn^{2+} addition (solid line) and after 15 min (open squares), 25 min (open circles), and 2 h (open stars) of Zn^{2+} addition. (b) Scattered light intensity and (c) fluorescence from 20 μM (hatched bar) and 10 μM (black bar) Aβ solutions. "Day 0" denotes measurements made immediately after the preparation of the solutions. "Day 1" denotes measurements made after 24 h. An increase of scattering after Zn^{2+} addition, followed by a reduction of both scattering and fluorescence with centrifugation, implies formation of larger particles upon Zn^{2+} addition. (d) 3D plot showing the kinetics of the size distribution in 4 μM Aβ solution before and after 8 μM Zn^{2+} addition. The horizontal axis on the right side indicates the incubation time of the solution in hours. The size distribution does not change with time or with Zn^{2+} addition, indicating that 8 μM Zn^{2+} does not affect subsaturated Aβ solutions.

empty squares). After 25 min the average size increases further (to ∼380 nm), but the population amplitude decreases (Figure 2a, empty circles). However, after 2 h of zinc addition the soluble aggregate species disappear and only the monomer-like species remains (Figure 2a, empty stars). Hence, the FCS measurements suggest that larger aggregates form upon zinc addition and that these aggregates disappear later through sedimentation. We further verify these observations by monitoring the turbidity and the soluble Aβ content of the solutions upon zinc addition. We prepared Aβ solutions of initial concentrations of 10 and 20 μM. The soluble Aβ concentration is measured by the intensity of the tyrosine fluorescence, and the population of the large aggregates is gauged by the turbidity (measured here by the intensity of 350 nm light scattered perpendicular to the excitation in a fluorimeter). The data are shown as bar graphs in Figure 2b (scattered light intensity) and Figure 2c (tyrosine fluores-cence). The hatched and the black bars represent measure-ments from 20 and 10 μM Aβ solutions, respectively. "Day 0" corresponds to measurements performed at time 0, and

"Day 1" corresponds to measurements done after 24 h of preparation of the solutions. The turbidity of both the solutions increase after 1 day (Figure 2b), signifying the formation of larger sized particles with time. The scattering increases more than 2-fold within a few minutes of addition of 8 μM Zn^{2+} to the Aβ solutions. However, the scattered intensity decreases to less than its initial value after centrifugation at 2000g for 20 min. We infer that addition of Zn^{2+} enhances the formation of larger sized particles by lowering the barrier toward the aggregation of the larger soluble aggregates. Tyrosine fluorescence measurements (Figure 2c) show that Zn^{2+} addition increases the precipita-tion of Aβ. Taken together, the FCS, scattering, and fluorescence measurements imply that Zn^{2+} induces the formation of larger aggregates which then precipitate faster. However, the Aβ concentration remaining after the addition of Zn^{2+} is still above the saturation concentration of 4 μM (see Figure 2c; the concentration remaining is equivalent to 11 and 6 μM for the solutions with initial concentrations 20 and 10 μM, respectively).
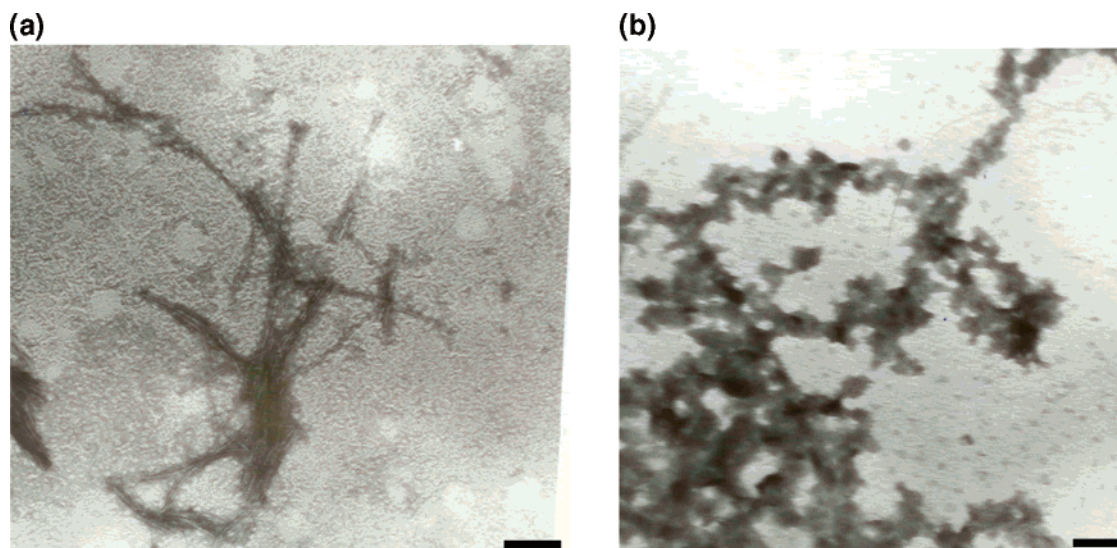
(a)

(b)

FIGURE 3: Amorphous aggregation of Aβ due to interaction with Zn^{2+}. EM images of the aggregates from 50 μM Aβ solution in the absence (a) and in the presence (b) of 8 μM Zn^{2+}. The aggregates in the absence of Zn^{2+} are fibrillar. However, in the presence of Zn^{2+}, we exclusively observe nonfibrillar aggregates. Scale bar 100 nm.

Any depression of the saturation concentration of Aβ by 8 μM Zn^{2+} can be sensitively probed by a solution near saturation. We perform FCS measurements on a 4 μM Aβ solution and follow the kinetics of the particle distribution after addition of 8 μM Zn^{2+}, similar to the measurements described in Figure 2a. The size distributions measured at different time points are shown in a 3D graph (Figure 2d). The 4 μM Aβ solution shows a distribution with a single peak situated at 2 nm. The distribution does not change over 60 h, as expected for a subsaturated solution. The addition of Zn^{2+} to this solution does not produce any change in the distribution over the next 2 h. Hence, 8 μM Zn^{2+} does not affect the monomeric population in subsaturated Aβ solution.

In a supersaturated solution, once an aggregate is formed, it is expected to grow. However, the spontaneous aggregation to form larger precipitable protofibrils is slow, and the soluble aggregates are stable for days (*10*). It appears that Zn^{2+} allows access to a much faster precipitation route, perhaps through less ordered structures. We expect the conformation of the early immature precipitates to manifest this difference. We examine the conformation of the aggregates of a 50 μM Aβ solution after 24 h of its preparation with electron microscopy (EM). The EM images of the aggregates precipitated without Zn^{2+} (Figure 3a) show many long and thin fibrils. We then perform EM measurements on the aggregates of a 50 μM Aβ solution in which 8 μM Zn^{2+} has been added 2 h after the preparation of the Aβ solution. The EM images (Figure 3b) of these aggregates are very different and show an amorphous network of small, apparently globular, aggregates. The radii of these globular particles are mostly in the range of ≥30 nm. These precipitates appear to have resulted from nonspecific and nondirectional association of soluble globular aggregates.

If this quick precipitation is induced by Zn^{2+} binding, then chelating the Zn^{2+} back from the Aβ molecules should reverse this effect (*28*). We introduce the metal chelator EDTA to check the reversibility of the Zn^{2+}−aggregate interaction. We add 8 μM Zn^{2+} to a 10 μM Aβ solution 10 h after its preparation and add 20 μM EDTA to the mixture 1 h after that. The size distribution before Zn^{2+} addition

(triangles), after Zn^{2+} addition (squares), and after EDTA addition (circles) is shown in Figure 4a. Initially the distribution contains large aggregates, and expectedly, they disappear after the addition of Zn^{2+}. However, the size distribution changes within a few minutes of EDTA application, with the large soluble aggregates coming back into the solution. We then test how long the precipitation remains reversible. We repeat the experiment with an Aβ solution which has been incubated with Zn^{2+} for 12 h. Figure 4b shows the size distributions obtained from these solutions. The size distributions from the solution incubated without (triangles) and with (squares) Zn^{2+} are as expected. However, addition of EDTA (circles) this time causes no substantial change. It is clear that the soluble aggregates precipitated by Zn^{2+} become stable within 12 h and do not come back into the solution even after EDTA addition.

We then ask whether the soluble aggregates observed in our experiments are toxic and whether their elimination has any bearing on Aβ toxicity. We tested the toxicity of the Aβ solutions whose size distribution is reported in Figure 1 on a set of primary cultured raphe neurons from rat brains. Cell death was measured using fluorescent DNA intercalating dyes Hoechst 33342 (which labels all the cells) and PI (which labels only the dead cells). Cells were visualized with a fluorescence microscope, and the extent of cell death is calculated as the ratio of PI- to Hoechst-labeled cells. Different sets of cells were incubated with 2 μM Aβ solution and also in a control solution (containing no Aβ) for 9 h. With 2 μM Aβ solution 11% cell death ($\sigma_{SEM} = 1.1$, $n = 448$) is observed, which is similar to that of the control, where 8% of the cells die ($\sigma_{SEM} = 1.1$, $n = 628$) (Figure 5c). This shows that either the species generated by a subsaturated solution are not significantly toxic or 2 μM is too low to cause toxicity. We then incubated the cells with 10 μM Aβ solutions with and without 8 μM Zn^{2+}; a representative set of 10 μM Aβ-treated cells are shown in Figure 5a. Three images are superimposed in this figure. The transmission image is seen in gray, the Hoechst fluorescence is seen in red, and the PI fluorescence is green. Colocalization of red and green shows up as yellow-orange. Figure 5b shows a
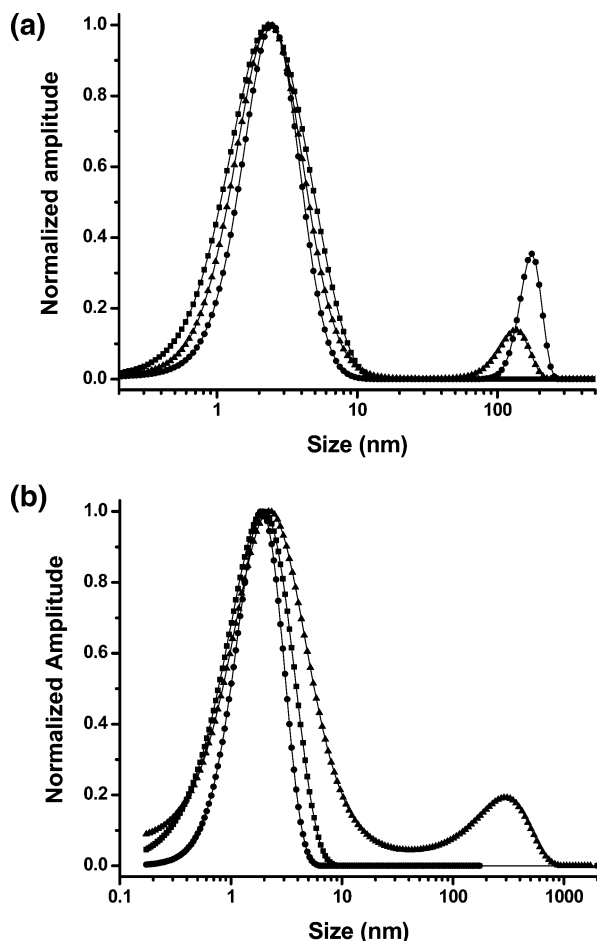
(a)

(b)

FIGURE 4: Solubilization of Zn^{2+}-induced precipitates of $A\beta$ by EDTA. (a) Size distributions obtained from 10 μM $A\beta$ after 10 h of preparation of the solution (triangles), 30 min after addition of 8 μM Zn^{2+} (squares), and then 20 min after addition of 20 μM EDTA (circles) in the same solution. The abscissa is calibrated with reference to Rhodamine B. The ordinate shows the population weighted by the square of the brightness of individual particles. The larger soluble aggregates which precipitated due to Zn^{2+} reappear in the solution with addition of EDTA. (b) Size distributions from $A\beta$ solution incubated with 8 μM Zn^{2+} for 12 h, before addition (squares) and 1 h after addition (circles) of 20 μM EDTA. The size distribution from an $A\beta$ control solution is shown in triangles. The squares and circles curves are very similar; this signifies the null effect of EDTA on the matured precipitates.

similar image for cells treated with both 10 μM $A\beta$ and Zn^{2+}. Cell death in the presence of 10 μM $A\beta$ (no Zn^{2+}) is 58% (incubation time 9 h, standard error of the mean $\sigma_{SEM} = 13.8$, number of cells $n = 1723$), whereas that in the presence of both Zn^{2+} and $A\beta$ is 13% ($\sigma_{SEM} = 13.9$, $n = 1035$) (Figure 5c). The asterisk on the error bar in Figure 5c indicates that the cell death is significantly different ($P < 0.05$) between samples treated with 10 μM $A\beta$ (without Zn^{2+}) and the other three. The difference between Zn^{2+}-treated and the control cells is not statistically significant.

We then test whether Zn^{2+} has a similar effect at a much lower stoichiometric ratio. We repeat these experiments with 8 μM Zn^{2+} and 50 μM $A\beta$. FCS measurements show that the larger aggregates are eliminated even at this low stoichiometric ratio (data not shown). We then assay cell death with these solutions. Since cell death is faster at this $A\beta$ concentration, cells were incubated only for 4 h. Cell death in the presence of 50 μM $A\beta$ (no Zn^{2+}) is 40% (incubation time 4 h, $\sigma_{SEM} = 7.7$, $n = 2626$), whereas that

in the presence of both 8 μM Zn^{2+} and 50 μM $A\beta$ is 5% ($\sigma_{SEM} = 1.1$, $n = 2056$). This value is similar to that of the controls, where 8% of the cells die ($\sigma_{SEM} = 2.6$, $n = 1438$) (Figure 5d). The asterisk on the bar in Figure 5d indicates that the cell death is significantly different ($P < 0.0005$) between samples treated with $A\beta$ only and the other two. The results establish that Zn^{2+}-induced precipitation of the soluble aggregates leads to an elimination of $A\beta$ toxicity.

DISCUSSION

The larger soluble aggregates (size >10 nm) are observed only in the supersaturated solutions. Even in nearly saturated solutions (4 μM), large particles are never observed (at least within 60 h of preparation), and they do not appear even after the addition of Zn^{2+} (Figure 2d). We conclude that the formation of these particles is inherently linked to precipitation, and they represent intermediates in the aggregation pathway. The comparatively wider size distribution of the smaller particles also indicates that a considerable fraction of these are also on the pathway to aggregation. We note here that the measured saturation concentration of 4 μM falls within the broad range (0.2−40 μM) reported by different groups (*10, 29−32*). The variations are possibly due to different buffer solutions and incubation temperatures used by the different groups.

In vitro, a Zn^{2+} concentration of 1 mM promotes $A\beta$ aggregation by >100-fold (*16*). Here we find that Zn^{2+} at <10 μM concentration selectively accelerates the precipitation of the intermediates, but does not change the final levels of precipitation. This is consistent with earlier observations that in the presence of such concentrations of Zn^{2+} the saturation concentration remains unaffected (*14*). Taking these observations together, we conclude that 8 μM Zn^{2+} lowers the kinetic barrier toward the formation of the precipitates, without altering the overall thermodynamics of precipitation.

It is interesting to speculate how Zn^{2+} actually accelerates the precipitation process. It has been suggested that Zn^{2+} binds to $A\beta$ primarily through His13 and His 14, with other residues bearing side-chain amine groups playing a possible role (*33*). AFM and EM studies of the precipitates of $A\beta_{13-21}$K16A have suggested that, in the presence of Zn^{2+}, growth perpendicular to the long axis is facilitated by a Zn^{2+} coordinating with His13 of one $A\beta$ molecule and His14 of another, with Zn^{2+} effectively acting as a glue between the different strands of $A\beta$ (*34*). It is also known that Zn^{2+} addition may result in nonfibrillar precipitates (*35*). In our case we hypothesize that this lateral growth would quickly increase the size of the $A\beta$ aggregates in solution, driving their precipitation. The increase in the aggregate size immediately after the addition of Zn^{2+} (Figure 2a) and the increase of scattering (Figure 2b) are consistent with this scenario. This rapid nonspecific lateral association also leaves its imprint on the freshly precipitated $A\beta$ aggregates, as observed through EM (Figure 3b). The image appears as a network of the globular particles, which have individual sizes
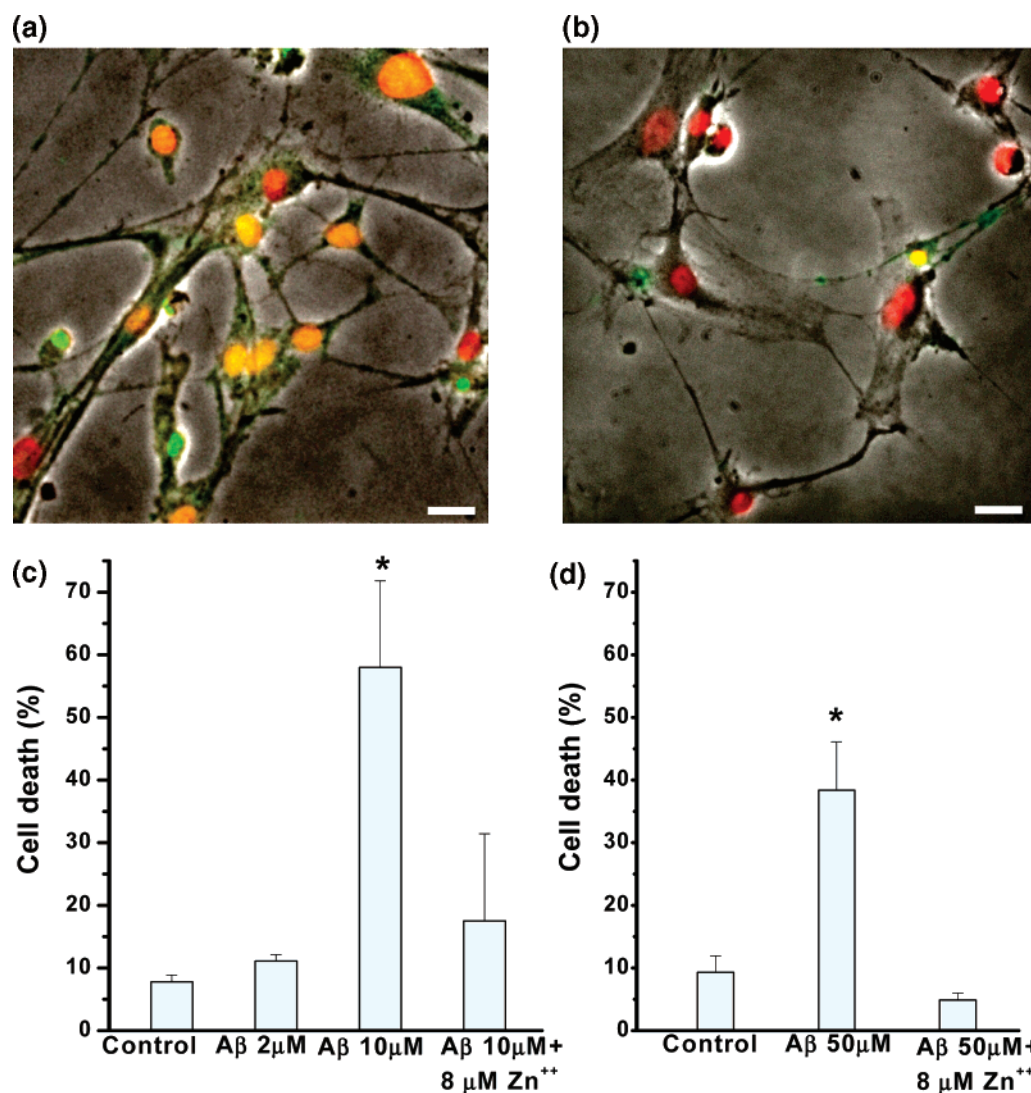
FIGURE 5: Elimination of the soluble aggregates renders Aβ nontoxic. Primary cultured raphe neurons 4 h after treatment with 50 μM Aβ in the absence (a) and in the presence (b) of 8 μM Zn^{2+}. Transmission (black and white), Hoechst 33342 fluorescence (red), and PI fluorescence (green) images are superimposed. Colocalization of green and red shows up as yellow-orange. Higher PI labeling in cells without Zn^{2+} implies greater cell death. The histogram plot shows the percentage of cell death of (c) cells incubated for 9 h in control (no Aβ, no Zn^{2+}), 2 μM Aβ, 10 μM Aβ, and 10 μM Aβ + Zn^{2+} solutions and (d) cells incubated for 4 h in control, 50 μM Aβ, and 50 μM Aβ + Zn^{2+} solutions. Scale bar 20 μm.

on the order of ≥ 30 nm, consistent with the FCS measurement made before Zn^{2+} addition (Figure 1d). This would also imply that stripping the Zn^{2+} from Aβ will bring these particles back into solution. However, if 8 μM Zn^{2+} does not alter the thermodynamics of precipitation, then removing Zn^{2+} after a sufficiently long time should not alter Aβ precipitation. Given enough time, the axial growth (which is presumably less dependent on Zn^{2+}, since long and thin amyloid fibrils spontaneously form without any addition of Zn^{2+}) should become sufficient to keep the particles precipitated. Our results show that this is indeed the case. Administration of EDTA within an hour of precipitation actually brings a large population of soluble aggregates back into the solution (Figure 4a). On the other hand, similar EDTA administration 12 h after Zn^{2+}-induced precipitation fails to reverse the precipitation (Figure 4b). We note that the accessibility of the Zn^{2+} binding site to EDTA may decrease with time, and this could be another reason for this lack of reversibility. However, even this alternative possibil-

ity is consistent with a Zn^{2+}-independent growth of the precipitates.

Our results shed light on the finding that Zn^{2+} at low (<50 μM) levels reduces Aβ toxicity (19−22). This has invited multiple explanations, such as the suppression of reactive oxygen species by Zn^{2+} (21), the inhibition of the Ca^{2+} current through channels formed by Aβ oligomers (22, 36, 37), the enhancement of Na^+/K^+ ATPase activity (19), and the inhibition of the toxic Aβ−Cu complex formation (21). Our results provide a simple alternative explanation: Zn^{2+}-induced rapid precipitation of the soluble Aβ aggregates abolishes Aβ toxicity. This explanation is in line with earlier findings that alterations of Aβ aggregation kinetics, without a disruption of the aggregation process per se, can be sufficient for reducing Aβ toxicity (38). At concentrations much higher than what is used here, Zn^{2+} increases the overall amount of the precipitation (15, 16), which may have its own deleterious effects (39). Our results can have significant implications for AD. Though the concentration

of Zn^{2+} used in our in vitro studies is relatively high compared to in vivo concentrations, this needs to be considered in the context of the much higher saturation concentration of Aβ in vitro (a few micromolar vs a few picomolar (*6*, *10*)). Also, the concentration of zinc in the brain can reach substantial levels ($\sim$2 μM) (*40*), and synaptic activity releases Zn^{2+} in the extracellular medium, transiently increasing its level in the vicinity (*41*). Interestingly, Zn^{2+} levels in the cerebrospinal fluid are lower in AD patients compared to age-matched controls (*40*). We hypothesize that Zn^{2+}-induced precipitation may be a natural mechanism which controls the toxicity of Aβ in vivo. Our results are relevant for the ongoing clinical trials for treating AD with metal ion chelators (*42*). Careful control of Zn^{2+} homeostasis in the brain, as opposed to aggressive Zn^{2+} chelation, may be the right approach for intervention in AD.

ACKNOWLEDGMENT

REFERENCES

1. Klein, W. L., Krafft, G. A., and Finch, C. E. (2001) Targeting small Abeta oligomers: the solution to an Alzheimer's disease conundrum? *Trends Neurosci. 24*, 219−224.
2. Lashuel, H. A., Hartley, D., Petre, B. M., Walz, T., and Lansbury, P. T., Jr. (2002) Neurodegenerative disease: amyloid pores from pathogenic mutations, *Nature 418*, 291.
3. Hoshi, M., Sato, M., Matsumoto, S., Noguchi, A., Yasutake, K., Yoshida, N., and Sato, K. (2003) Spherical aggregates of beta-amyloid (amylospheroid) show high neurotoxicity and activate tau protein kinase I/glycogen synthase kinase-3beta, *Proc. Natl. Acad. Sci. U. S. A. 100*, 6370-6375.
4. Hartley, D. M., Walsh, D. M., Ye, C. P., Diehl, T., Vasquez, S., Vassilev, P. M., Teplow, D. B., and Selkoe, D. J. (1999) Protofibrillar intermediates of amyloid beta-protein induce acute electrophysiological changes and progressive neurotoxicity in cortical neurons, *J. Neurosci. 19*, 8876−8884.
5. Cleary, J. P., Walsh, D. M., Hofmeister, J. J., Shankar, G. M., Kuskowski, M. A., Selkoe, D. J., and Ashe, K. H. (2005) Natural oligomers of the amyloid-beta protein specifically disrupt cognitive function, *Nat. Neurosci. 8*, 79−84.
6. Lue, L. F., Kuo, Y. M., Roher, A. E., Brachova, L., Shen, Y., Sue, L., Beach, T., Kurth, J. H., Rydel, R. E., and Rogers, J. (1999) Soluble amyloid beta peptide concentration as a predictor of synaptic change in Alzheimer's disease, *Am. J. Pathol. 155*, 853−862.
7. Murphy, R. M., and Pallitto, M. M. (2000) Probing the kinetics of beta-amyloid self-association, *J. Struct. Biol. 130*, 109−122.
8. Tjernberg, L. O., Pramanik, A., Bjorling, S., Thyberg, P., Thyberg, J., Nordstedt, C., Berndt, K. D., Terenius, L., and Rigler, R. (1999) Amyloid beta-peptide polymerization studied using fluorescence correlation spectroscopy, *Chem. Biol. 6*, 53−62.
9. Walsh, D. M., Klyubin, I., Fadeeva, J. V., Cullen, W. K., Anwyl, R., Wolfe, M. S., Rowan, M. J., and Selkoe, D. J. (2002) Naturally secreted oligomers of amyloid beta protein potently inhibit hippocampal long-term potentiation in vivo, *Nature 416*, 535−539.
10. Sengupta, P., Garai, K., Sahoo, B., Shi, Y., Callaway, D. J., and Maiti, S. (2003) The amyloid beta peptide (Abeta(1-40)) is thermodynamically soluble at physiological concentrations, *Biochemistry 42*, 10506−10513.
11. Sengupta, P., Garai, K., Balaji, J., Periasamy, N., and Maiti, S. (2003) Measuring size distribution in highly heterogeneous systems with fluorescence correlation spectroscopy, *Biophys. J. 84*, 1977−1984.
12. De Felice, F. G., Vieira, M. N., Saraiva, L. M., Figueroa-Villar, J. D., Garcia-Abreu, J., Liu, R., Chang, L., Klein, W. L., and Ferreira, S. T. (2004) Targeting the neurotoxic species in Alzheimer's disease: inhibitors of Abeta oligomerization, *FASEB J. 18*, 1366-1372.
13. Klyubin, I., Walsh, D. M., Lemere, C. A., Cullen, W. K., Shankar, G. M., Betts, V., Spooner, E. T., Jiang, L., Anwyl, R., Selkoe, D. J., and Rowan, M. J. (2005) Amyloid beta protein immunotherapy neutralizes Abeta oligomers that disrupt synaptic plasticity in vivo, *Nat. Med. 11*, 556−561.
14. Garai, K., Sengupta, P., Sahoo, B., and Maiti, S. (2006) Selective destabilization of soluble amyloid beta oligomers by divalent metal ions, *Biochem. Biophys. Res. Commun. 345*, 210−215.
15. Bush, A. I., Pettingell, W. H., Multhaup, G., d Paradis, M., Vonsattel, J. P., Gusella, J. F., Beyreuther, K., Masters, C. L., and Tanzi, R. E. (1994) Rapid induction of Alzheimer A beta amyloid formation by zinc, *Science 265*, 1464−1467.
16. Esler, W. P., Stimson, E. R., Jennings, J. M., Ghilardi, J. R., Mantyh, P. W., and Maggio, J. E. (1996) Zinc-induced aggregation of human and rat beta-amyloid peptides in vitro, *J. Neurochem. 66*, 723−732.
17. Lovell, M. A., Robertson, J. D., Teesdale, W. J., Campbell, J. L., and Markesbery, W. R. (1998) Copper, iron and zinc in Alzheimer's disease senile plaques, *J. Neurol. Sci. 158*, 47−52.
18. Lee, J. Y., Cole, T. B., Palmiter, R. D., Suh, S. W., and Koh, J. Y. (2002) Contribution by synaptic zinc to the gender-disparate plaque formation in human Swedish mutant APP transgenic mice, *Proc. Natl. Acad. Sci. U. S. A. 99*, 7705−7710.
19. Lovell, M. A., Xie, C., and Markesbery, W. R. (1999) Protection against amyloid beta peptide toxicity by zinc, *Brain Res. 823*, 88−95.
20. Bishop, G. M., and Robinson, S. R. (2004) The amyloid paradox: amyloid-beta-metal complexes can be neurotoxic and neuroprotective, *Brain Pathol. 14*, 448−452.
21. Cuajungco, M. P., Goldstein, L. E., Nunomura, A., Smith, M. A., Lim, J. T., Atwood, C. S., Huang, X., Farrag, Y. W., Perry, G., and Bush, A. I. (2000) Evidence that the beta-amyloid plaques of Alzheimer's disease represent the redox-silencing and entombment of abeta by zinc, *J. Biol. Chem. 275*, 19439−19442.
22. Zhu, Y. J., Lin, H., and Lal, R. (2000) Fresh and nonfibrillar amyloid beta protein(1-40) induces rapid cellular degeneration in aged human fibroblasts: evidence for AbetaP-channel-mediated cellular toxicity, *FASEB J. 14*, 1244−1254.
23. Moreira, P., Pereira, C., Santos, M. S., and Oliveira, C. (2000) Effect of zinc ions on the cytotoxicity induced by the amyloid beta-peptide, *Antioxid. Redox Signal. 2*, 317−325.
24. Cuajungco, M. P., and Faget, K. Y. (2003) Zinc takes the center stage: its paradoxical role in Alzheimer's disease, *Brain Res. Brain Res. Rev. 41*, 44−56.
25. Sengupta, P., Balaji, J., and Maiti, S. (2002) Measuring diffusion in cell membranes by fluorescence correlation spectroscopy, *Methods 27*, 374−387.
26. Clause, B. T. (1993) The Wistar rat as a right choice: Establishing mammalian standards and the ideal of a standardized mammal, *J. History Biol. 26*, 329-349.
27. Bailey, N. (1995) *Statistical Methods in Biology*, 3rd ed., Cambridge University Press, Cambridge.
28. Huang, X., Atwood, C. S., Moir, R. D., Hartshorn, M. A., Vonsattel, J. P., Tanzi, R. E., and Bush, A. I. (1997) Zinc-induced Alzheimer's Abeta1-40 aggregation is mediated by conformational factors, *J. Biol. Chem. 272*, 26464−26470.
29. Harper, J. D., and Lansbury, P. T., Jr. (1997) Models of amyloid seeding in Alzheimer's disease and scrapie: mechanistic truths and physiological consequences of the time-dependent solubility of amyloid proteins, *Annu. Rev. Biochem. 66*, 385−407.
30. Hasegawa, K., Ono, K., Yamada, M., and Naiki, H. (2002) Kinetic modeling and determination of reaction constants of Alzheimer's beta-amyloid fibril extension and dissociation using surface plasmon resonance, *Biochemistry 41*, 13489−13498.
31. O'Nuallain, B., Shivaprasad, S., Kheterpal, I., and Wetzel, R. (2005) Thermodynamics of A beta(1-40) amyloid fibril elongation, *Biochemistry 44*, 12709−12718.
32. Hortschansky, P., Christopeit, T., Schroeckh, V., and Fandrich, M. (2005) Thermodynamic analysis of the aggregation propensity of oxidized Alzheimer's beta-amyloid variants, *Protein Sci. 14*, 2915−2918.
33. Miura, T., Suzuki, K., Kohata, N., and Takeuchi, H. (2000) Metal binding modes of Alzheimer's amyloid beta-peptide in insoluble aggregates and soluble complexes, *Biochemistry 39*, 7024−7031.
34. Dong, J., Shokes, J. E., Scott, R. A., and Lynn, D. G. (2006) Modulating amyloid self-assembly and fibril morphology with Zn-(II), *J. Am. Chem. Soc. 128*, 3540−3542.

35. Yoshiike, Y., Tanemura, K., Murayama, O., Akagi, T., Murayama, M., Sato, S., Sun, X., Tanaka, N., and Takashima, A. (2001) New insights on how metals disrupt amyloid beta-aggregation and their effects on amyloid-beta cytotoxicity, *J. Biol. Chem. 276*, 32293–32299.

36. Kawahara, M., Arispe, N., Kuroda, Y., and Rojas, E. (1997) Alzheimer's disease amyloid beta-protein forms Zn(2+)-sensitive, cation-selective channels across excised membrane patches from hypothalamic neurons, *Biophys. J. 73*, 67–75.

37. Lin, H., Bhatia, R., and Lal, R. (2001) Amyloid beta protein forms ion channels: implications for Alzheimer's disease pathophysiology, *FASEB J. 15*, 2433–2444.

38. Ghanta, J., Shen, C. L., Kiessling, L. L., and Murphy, R. M. (1996) A strategy for designing inhibitors of beta-amyloid toxicity, *J. Biol. Chem. 271*, 29525–29528.

39. Pike, C. J., Burdick, D., Walencewicz, A. J., Glabe, C. G., and Cotman, C. W. (1993) Neurodegeneration induced by beta-amyloid peptides in vitro: the role of peptide assembly state, *J. Neurosci. 13*, 1676–1687.

40. Molina, J. A., Jimenez-Jimenez, F. J., Aguilar, M. V., Meseguer, I., Mateos-Vega, C. J., Gonzalez-Munoz, M. J., de Bustos, F., Porta, J., Orti-Pareja, M., Zurdo, M., Barrios, E., and Martinez-Para, M. C. (1998) Cerebrospinal fluid levels of transition metals in patients with Alzheimer's disease, *J. Neural Transm. 105*, 479–488.

41. Frederickson, C. J., and Bush, A. I. (2001) Synaptically released zinc: physiological functions and pathological effects, *Biometals 14*, 353–366.

42. Ritchie, C. W., Bush, A. I., Mackinnon, A., Macfarlane, S., Mastwyk, M., MacGregor, L., Kiers, L., Cherny, R., Li, Q. X., Tammer, A., Carrington, D., Mavros, C., Volitakis, I., Xilinas, M., Ames, D., Davis, S., Beyreuther, K., Tanzi, R. E., and Masters, C. L. (2003) Metal-protein attenuation with iodochlorhydroxyquin (clioquinol) targeting Abeta amyloid deposition and toxicity in Alzheimer disease: a pilot phase 2 clinical trial, *Arch. Neurol. 60*, 1685–1691.

43. Cherny, R. A., Atwood, C. S., Xilinas, M. E., Gray, D. N., Jones, W. D., McLean, C. A., Barnham, K. J., Volitakis, I., Fraser, F. W., Kim, Y., Huang, X., Goldstein, L. E., Moir, R. D., Lim, J. T., Beyreuther, K., Zheng, H., Tanzi, R. E., Masters, C. L., and Bush, A. I. (2001) Treatment with a copper-zinc chelator markedly and rapidly inhibits beta-amyloid accumulation in Alzheimer's disease transgenic mice, *Neuron 30*, 665–676.